International Journal of Heat and Fluid Flow 53 (2015) 44–55

Contents lists available at ScienceDirect

International Journal of Heat and Fluid Flow

journal homepage: www.elsevier.com/locate/ijhff

Turbulent stresses and particle break-up criteria in particle-laden pipe flows

J.L.G. Oliveira [a,1], C.W.M. van der Geld [a,*], J.G.M. Kuerten [a,b]

[a] Department of Mechanical Engineering, Eindhoven University of Technology, P.O. Box 513, 5600 MB Eindhoven, The Netherlands
[b] Faculty EEMCS, University of Twente, The Netherlands

ARTICLE INFO

Article history:
Received 10 August 2014
Received in revised form 5 February 2015
Accepted 16 February 2015

Keywords:
3D-PTV
Particle-laden flow
Pipe flow
Turbulence
Break-up

ABSTRACT

Three-dimensional particle tracking velocimetry (3D-PTV) is applied to particle-laden pipe flows at Reynolds number 10,300, based on the bulk velocity and the pipe diameter. The effects of flow direction (upward or downward) and mean concentration (in the range 0.5×10^{-5}–3.2×10^{-5}) on the production of turbulence are assessed for inertial particles with a Stokes number equal to 2.3, based on the particle relaxation time and viscous scales. The turbulence production and the Kolmogorov constant, both measured for particle laden flows in upflow and downflow, allowed for the derivation of a break-up criterion as a function of the radial coordinate. This criterion predicts the maximum possible particle size before break-up may occur. It is shown that the maximum particle size is bigger at the pipe centerline than in the near-wall zone by more than a factor of 5. Flow direction affects the particle concentration profile, with wall peaking in downflow and core peaking in upflow. This affects both the residence time and the maximum particle size, the latter by 7%.

1. Introduction

The dispersion of inertial particles in turbulent flows is characterized by macroscopic phenomena such as a non-homogeneous distribution, large-scale clustering, and preferential concentration; see Wang and Maxey (1993). The distribution of the dispersed phase may be crucial in determining collision frequency, breakage efficiency, agglomeration, reaction rates, deposition and entrainment; see Marchioli et al. (2008). Many of these phenomena occur in practice in turbulent pipe flows, with applications ranging from pneumatic conveying systems and oil pipelines to chemical reactor design; see Kartusinsky et al. (2009). Accurate determination of inertial particle distributions is therefore of considerable interest, in particular when break-up may occur.

However, experimental data for inertial particles with a size exceeding the Kolmogorov length scale are scarce, while numerical work is mostly limited to point-force predictions, see Poelma et al. (2006). Attempts to predict turbulence augmentation or attenuation by particles in two-phase flows mostly utilize simplified models, see Gore and Crowe (1989), Hetsroni (1989) and Elgobashi (1994). Fully numerical computations of finite particles require significant memory and processing speed and only simple geometries with limited numbers of particles were studied, see Tryggvason et al. (2001). It appears that experiments are indispensable to reveal and understand the underlying physics of dispersed two-phase flows. However, most of the experimental studies of particle-laden flows concerned air with small solid particles, compared to the Kolmogorov length scale, and with a high mass density in turbulent wall-bounded flows, see Tsuji and Morikawa (1982), Tsuji et al. (1984), Kulick et al. (1994), Paris and Eaton (2001), Kussin and Sommerfeld (2002), Caraman et al. (2003), Yang and Shy (2005), Benson et al. (2005) and Borée and Caraman (2005). The dynamics and turbulent transport of near-neutrally buoyant particles in water was only recently experimentally examined, see Volk et al. (2011), but only for homogenous and isotropic turbulence. Only very few particle laden liquid flow experiments were performed in turbulent flow in a square channel; see Sato and Hishida (1996) and Suzuki et al. (2000), but only for a certain class of inertial particles and in channel flow. To the best of the authors' knowledge, experiments of this kind (turbulent liquid flows in pipes with almost neutrally buoyant solid particles) have only been performed by the present authors.

The control of particle break-up mechanisms plays an essential role in industrial processes, for example to prevent damage of starch particles, see Risso (2000). Ever since the pioneering work

* Corresponding author. Tel.: +31 402472923; fax: +31 402475399.
E-mail addresses: jorge.goes@ufsc.br (J.L.G. Oliveira), C.W.M.v.d.Geld@tue.nl (C.W.M. van der Geld).
[1] Present address: Mobility Center, Federal University of Santa Catarina, Joinville, SC 89218-000, Brazil.

http://dx.doi.org/10.1016/j.ijheatfluidflow.2015.02.001
0142-727X/

Nomenclature

a_1, a_2	fitting coefficients
A	area
C_D	drag coefficient
C_0	Kolmogorov constant
D	pipe diameter
D_{kk}	second order Lagrangian velocity structure function
d_p	particle diameter
$d_{p,max}$	maximum particle diameter in turbulent flows
f	Darcy friction factor
F	F-statistic
g	gravitational acceleration constant
i	bin number
j	photograph number
k	total number of radial bins; cylindrical coordinate components
K	number of parameters determined in the fit equation
m	total number of photographs
n	refractive index; measurement number
N_i	number of particles in a discrete radial bin
O_i	value for break-up criteria
$\hat{O}_i$	predicted value for break-up criteria
P_k	production of turbulent kinetic energy
Q	mean volumetric flow rate

Greek symbols

ε	turbulence dissipation rate
η	Kolmogorov length-scales
θ	azimuthal direction
μ	dynamic viscosity
ν	kinematic viscosity
ρ	mass density
τ	time
τ_c	Lagrangian correlation time

Subscripts

b	bulk
i	discrete radial position
f	fluid
IP	inertial particles
p	particle
r	radial coordinate
r_{max}	radial position for the maximum concentration found
r_s^2	correlation coefficient
R	pipe radius
R_Φ	ratio of the mean concentration in different measurement section volumes
Re_b	Reynolds number based on the bulk velocity and the pipe diameter
Re_p	particle Reynolds number based on the particle diameter and the terminal velocity
S_{km}	rate-of-strain tensor
St	Stokes number
u	fluctuating fluid velocity
u_{rms}	root-mean-square velocity of the turbulent carrier phase
u_τ	wall shear velocity
U	instantaneous fluid velocity
U_b	flow bulk velocity
U_{TV}	settling velocity of a particle in an infinite, stagnant pool of water
U_z	mean axial fluid velocity
$v_{p,z}$	mean axial inertial particle velocity
$V_{bin\ i}$	volume of a bin
$V_{particle}$	volume of a particle
We_{crit}	critical value of the Weber number
x	value of a measured quantity; space coordinate
x_j	Cartesian coordinate system
τ_f	fluid time-scale based on viscous scales
τ_k	Kolmogorov time-scale
τ_p	relaxation time for particles in stationary flow
σ	surface tension coefficient
σ_m	standard error
Φ_v	particle volumetric concentration (–)
$\Phi_{v,max}$	maximum concentration found in a discrete bin
z	streamwise coordinate
1S	single-phase flow
2S	tracers in two-phase flow

of Hinze (1956), break-up in turbulent flow has been related to turbulent stresses and turbulence dissipation. Since turbulent pipe flow is inhomogeneous, it stands to reason to expect that the break-up criterion depends on the distance to the center of the pipe. It is the purpose of the present study to investigate whether this is indeed the case or not, and to quantify break-up criteria for particle-laden turbulent pipe flow.

To this end, 3D-PTV is applied at Reynolds number, Re_b, 10,300, based on the bulk velocity and the pipe diameter. The experimental setup allows for the simultaneous measurement of particle and fluid statistics in both upward and downward vertical flows. The influence of mean volumetric concentration of inertial particles on turbulence production is measured in the range 0.5×10^{-5}–3.2×10^{-5}. Inertial particles with a diameter equal to 0.8 mm are chosen. The mass density of these particles (1050 kg/m^3) slightly exceeds the mass density of the carrier fluid (1000 kg/m^3).

Next to the inertial particles, tracers are used to measure turbulence characteristics of the carrier fluid. In order to derive a break-up criterion of the form given by Hinze (1956), the turbulence dissipation rate and the Kolmogorov constant have to be known. The former can be estimated from the turbulence production, while the latter can be determined from the Lagrangian velocity correlation function, both in particle-laden flow. The turbulence production depends on the cross component of the Reynolds stress tensor and the mean axial velocity. Therefore, the dependence of mean axial velocity, cross-component of the Reynolds stress tensor and Lagrangian velocity correlation function on the radial coordinate are determined for up- and downflow within the given range of concentration of inertial particles. With the estimations obtained by measurements of turbulence characteristics, the maximum particle diameter that can occur without being torn apart is related to a critical Weber number. The critical Weber number is a threshold Weber number that relates bonding forces, classically represented by a surface tension coefficient, to fluid dynamic stresses exerted by the fluid on the particle in motion. In the case of particles also a surface tension coefficient is present, but it is smaller and does not fully represent the bonding forces that keep the particle intact. In this case an effective surface tension coefficient might be more appropriate. Previous studies on steam injection in a channel with water and starch particles have shown that starch particles can become distorted or even broken at high shear rates and at high temperatures; see Clerx et al. (2013), for example. Apparently, a critical Weber number of a kind can be applied also to solids. If the effective

surface tension coefficient is by definition representing the bonding forces of a particle, the corresponding Weber number can be used for break-up prediction.

The structure of the paper is as follows. In Section 2, the experimental setup and the description of the particle-laden experimental conditions are given. All experimental results are presented in Section 3. Section 3.1 deals with the concentration profile of the inertial particles. The mean axial velocity profiles for carrier and dispersed phases are shown in Section 3.2. Results of the cross-component of the Reynolds stress tensor are presented in Section 3.3. In Section 3.4, turbulence production results are shown. The determination of a direction-dependent Kolmogorov constant is done in Section 3.5. A break-up criterion for pipe flow at $Re_b = 10{,}300$ is derived in Section 4. Finally, conclusions are drawn in Section 5.

2. Experimental setup

2.1. Test rig

Turbulent particle-laden pipe flows have been created in a water loop driven by a centrifugal pump; see Fig. 1. The in-line 3 kW centrifugal pump of type DPV18-30, manufactured by "Duijvelaar pompen", allows Reynolds numbers, based on the bulk velocity, U_b, and pipe diameter, D, in the range 10^3–10^5.

A set of valves is arranged in such a way that downward and upward vertical flows are possible. In upward flow, a frequency controller permits fine-tuning of the Reynolds number by adjusting the mass flow rate in the measurement section. In downward flow, the mass flow rate is adjusted by controlling the pressure drop over a valve.

The mass flow rate is measured by means of a Micro Motion Elite CMF300 mass flow and mass density meter, whose inaccuracy is less than 0.5% of the registered flow rate. A water reservoir (tank I), located at the bottom of the setup, contains about 2 m^3 of water. This value facilitates water temperature stabilization and Reynolds number control. During a test-run, the temperature was essentially constant, varying typically only 0.1 °C.

Submerged pumps are placed in the reservoir tanks at the bottom and at the top of the setup in order to promote homogeneous dispersion of the added tracers and inertial particles. The volume of the top tank is smaller, ≈0.15 m^3, facilitating control of the concentration of particles.

The measurement section consists of a glass pipe to ensure optical accessibility. A water-filled rectangular glass box around the pipe minimizes optical distortions. The pipe diameter is chosen relatively large, 100 mm inner diameter, because measurements at high Reynolds numbers are required. For a certain Reynolds number, bulk velocities are lower for higher tube diameters, which is advantageous for the acquisition of Lagrangian statistics.

Flow straighteners, tube bundle conditioners of ISO 5167-1:1991, see Miller (1996), are employed to remove strong secondary flow effects. For upward flow, bundle conditioner I is placed downstream of a 90° bend; see Fig. 1. Bundle flow straightener I consists of a set of pipes with an internal diameter of 10 mm and an approximate length of 50 cm. It is constructed in such way that it can be replaced by a straight pipe section. For downward flow, bundle conditioner II is placed downstream of the bottom of tank II in the pipe that conducts the flow to the test section; see Fig. 1. Bundle flow straightener II consists of a set of pipes with an internal diameter of 5 mm and an approximate length of 40 cm. Similarly as bundle conditioner I, it can also be replaced by a straight pipe section.

Three "HighSpeedStar" cameras with 12 bit grayscale CMOS sensor and a resolution of 1024 × 1024 pixels have been utilized to capture almost instantaneous 3D particle positions in an approximate measurement volume of 1 × 1 × 1 dm^3. The cameras can record at 1000 Hz at full resolution, but were operated at 50 Hz to maximize the flow measurement time. Recordings are performed until the internal memory of the cameras becomes full during approximately 2 min. The maximum physically relevant frequencies are about 12 Hz for $Re_b = 10300$, making a 50 Hz sampling rate sufficient according to the Nyquist theorem.

Settings of cameras and lens arrangement were properly chosen in order to obtain sharp images of moving particles. While a minimum depth of field must be guaranteed to obtain sharp recordings in the whole volume of the measurement section, a minimum field of view is needed to obtain trajectories long enough to measure all relevant flow scales. For the present experiment, the settings can be summarized as:

- Sensor resolution 1 pixel = 17 μm^2.
- Focal length of 105 mm.
- Exposure time of 20 μs.
- Distance from the lens to the object of roughly 800 mm.

An in-situ calibration method has been utilized to transform the two-dimensional pixel information of each camera to world coordinates. A calibration unit precisely moves a grid with regular inter-spaced points throughout the measurement volume to certain positions, with high reproducibility. The bigger and well resolved the volume covered by the calibration plate, the smaller interpolation and extrapolation errors of the calibration functions are.

Calibration and flow measurement images were processed in order to make files, which contain time reference and spatial positions of individual particle trajectories. The magnification of a single lens was arranged such that 100 μm corresponds to one pixel width. The center of the particles is reconstructed from three views, given by the three corresponding camera recordings, and the resulting maximum triangulation error turns out to be of the order of 40 μm. The image projection area of particles and the light intensity captured by a camera pixel once light is reflected from particle surfaces allow to separate flow images with only particles (tracers and inertial particles) from the background noise. An important difference with the 3D-PTV procedure as applied by Oliveira et al. (2013) is the present use of imaging filters of Davis software which could segregate flow images with only inertial particles or only flow tracers. This task is facilitated by the imaging projection area of inertial particles on the camera sensor exceeding the projection area of tracers by a factor of 16. The uncertainty in the magnitude of the velocity vector obtained from two consecutive positions is for both tracers and particles about 0.06 mm/s. More information about the particle tracking algorithm used to obtain trajectories of tracers and inertial particles and the trajectory analysis method of individual particle trajectories is given by Oliveira et al. (2013) and Oliveira (2012). Additional descriptions of the mechanical construction for camera support and reproducible calibration, illumination and recording apparatus have already been reported before Oliveira et al. (2013), Oliveira (2012), Walpot et al. (2006).

2.2. Properties of applied particles

Properties of polystyrene particles applied in the present particle-laden experiments are given in Table 1. The fluid time-scale τ_f in the Stokes number, St, is based on viscous scales; see info below Table 1. The fluid length-scale is the Kolmogorov scale for fully developed single-phase pipe flow at $Re_b = 10300$ as computed from DNS results by Veenman (2004). The Kolmogorov length is about 0.6 mm in the pipe core and 0.2 mm at the wall

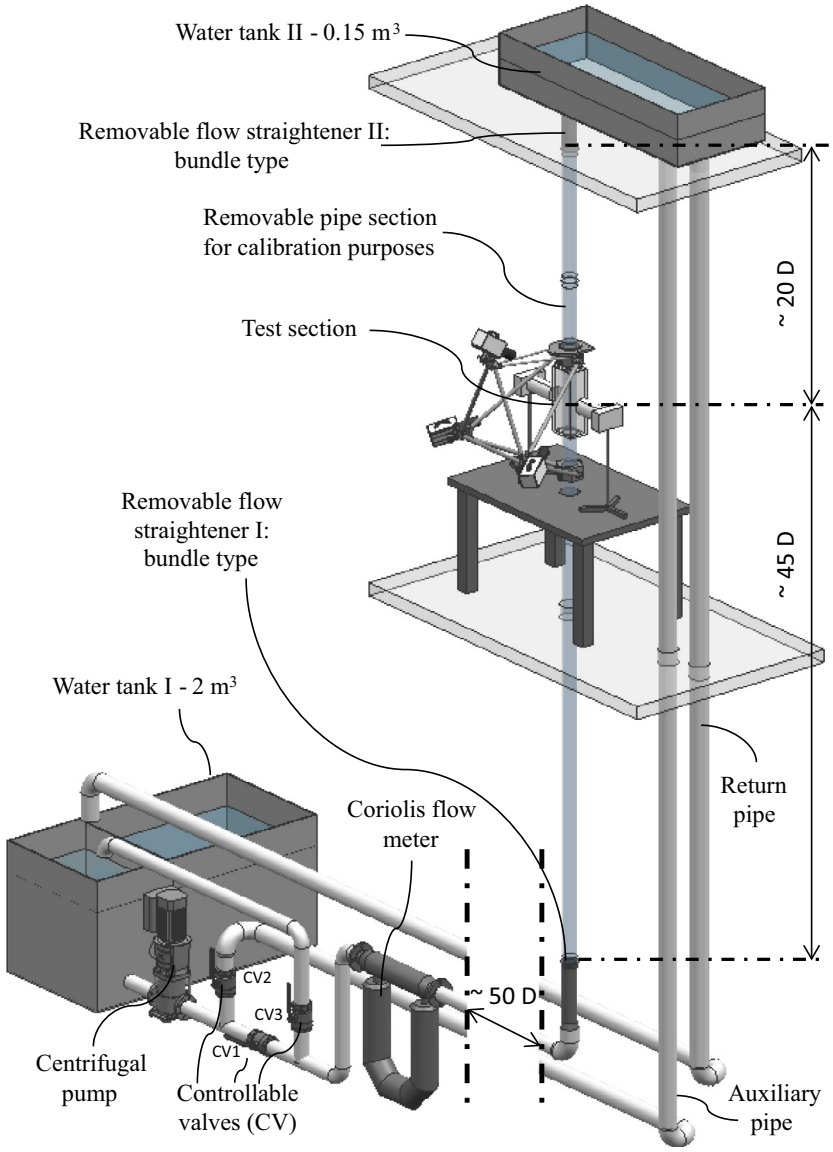

Fig. 1. Schematic of the 3D-PTV experimental setup for downward or upward particle-laden pipe flow.

Table 1
Properties of particles applied in the present particle-laden experiment.

Particles	Mass density (kg/m³)	Diameter d_p (mm)	Terminal velocity, U_{TV}[a] (mm/s)	Re_p[a]	$St = \tau_p/\tau_f$[b]	Length-scale ratio: d_p/η[c]
Flow tracers	1050	0.2	1.0	0.18	0.14	0.33–1
Inertial particles	1050	0.8	10.2	7.76	2.31	1.33–3.5

[a] Settling velocity of a particle in an infinite, stagnant pool of water.
[b] Fluid time-scale is based on viscous scales as given by: $\tau_f = \nu/u_\tau^2$. For $Re_b < 10^5$, the wall shear velocity can be estimated as $u_\tau = (U_b^2 f/8)^{1/2}$ with $f = a\, Re_b^{-m}$, $m = 0.25$ and $a = 0.316$; see van der Geld (2002). τ_f is roughly 28 ms.
[c] Kolmogorov length-scales for a fully developed single-phase pipe flow at $Re_b = 10{,}300$ as computed from the DNS code developed by Walpot et al. (2006): ≈0.60 mm at pipe centerline and ≈0.2 mm close to the wall.

region. For evaluation of the particle timescale, τ_p, the relaxation time for particles in stationary flow is used; see Albrecht et al. (2003):

$$\tau_p = \frac{d_p^2 \rho_p}{18\mu}\left(1 + \frac{0.5\rho_f}{\rho_p}\right) \tag{1}$$

where μ is the dynamic viscosity, d_p is the particle diameter and ρ_p and ρ_f are the mass densities of particles and fluid, respectively. A relaxation time of $\tau_p \approx 4$ ms is obtained for the tracers. Note that the fluid inertia is accounted for by the added mass coefficient 0.5 which close to a wall is increased to about 0.7; see van der Geld (2002).

The terminal velocity specified in Table 1 is attained in quiescent fluid when gravitational and drag forces are in equilibrium:

$$U_{TV} = \left[\frac{4(\rho_p - \rho_f) d_p g}{3 C_D \rho_f}\right]^{0.5} \tag{2}$$

where g is the gravitational acceleration constant and C_D the drag coefficient. The latter is a function of the particle Reynolds number, $Re_p = d_p|U_{TV}|/\nu$, which is based on the particle diameter and the terminal velocity. In the Stokes regime, C_D is given by Eq. (3). For $1 < Re_p < 1000$, Schiller and Naumann (1935) proposed a correlation for C_D given by Eq. (4):

$$C_D = \left(\frac{24}{\mathrm{Re}_p}\right);\ \mathrm{Re}_p < 1 \tag{3}$$

$$C_D = \left(\frac{24}{\mathrm{Re}_p}\right)\left(1 + \frac{1}{6}\mathrm{Re}_p^{2/3}\right);\ 1 < \mathrm{Re}_p < 1000 \tag{4}$$

A value for U_{TV} is obtained by an iterative computation using Eq. (2) and Eq.'s (3) or (4). Since the bulk flow velocity, U_b, is approximately 100 mm/s, the ratio U_b/U_{TV} is on the order of 10^2 for seeding particles, see Table 1. Since $U_b \gg U_{TV}$, $\tau_p < \tau_f$ and $d_p < \eta$, the employed seeding particles work well as flow tracers. For *inertial particles*, the ratio U_b/U_{TV} is on the order of 10, $\tau_p > \tau_f$ and $d_p > \eta$. Therefore, *inertial particles* have significant inertial characteristics to not behave as tracers.

2.3. Experimental conditions

Downward and upward vertical flows have been measured at the same bulk Reynolds number, Re_b. The bulk velocity of each flow, U_b, was adapted to temperature changes to keep $Re_b \approx 10{,}300$. Single-phase flows serve as a reference for two-phase flows.

Particle-laden flows with mean concentrations, $\langle \Phi_v \rangle$, ranging from 0.5×10^{-5} to 3.2×10^{-5} have been tested. The presence of flow conditioner I, see Fig. 1, assured fully developed pipe flow in upflow. In downward flows, the condition of fully developed flow was nearly satisfied, as will be shown below.

Only tracers are employed in single-phase flow measurements, while tracers and inertial particles are added to the water flow in particle-laden measurements. Mean concentration of tracers less than 10^{-6} is applied to each experiment. Properties of inertial particles (volume and mass density) are selected with the aim of testing particle-laden flows which have a characteristic root-mean-square velocity representative of the turbulent carrier phase, u_{rms}, and the terminal velocity of the dispersed phase, U_{TV}, of the same order of magnitude: $u_{rms}/U_{TV} \approx \mathrm{O}(1)$.

A particle-laden experimental case is represented here by a number (1 or 2) which indicates the flow direction and a letter (A, B or C), indicating the applied mean concentration of inertial particles. A summary of the tested particle-laden cases is shown in Table 2. The reference single-phase flows are specified by 1S or 2S.

Table 2
Summary of the single-phase and particle-laden flow experiments. All experimental runs have been performed at $Re_b = 10{,}300$.

Case	Flow direction	$\langle \Phi_v \rangle \cdot 10^{-5}$
1S	Upward	0
1A	Upward	0.5
1B	Upward	1.4
1C	Upward	3.2
2S	Downward	0
2A	Downward	1.8
2B	Downward	2.8

3. Results

3.1. Concentration profiles of inertial particles

The distribution of the dispersed phase is crucial in defining the break-up efficiency and in defining a correction factor for the break-up rate. Accurate determination of inertial particle distributions is therefore of considerable interest, in particular to evaluate the effect of flow direction (upflow or downflow) on the concentration profiles of the dispersed phase. The experimental determination of tracer and inertial particle distributions is described below.

The number of tracer trajectories measured in the range $r/R = 0.6$ to 1 decreases with increasing r. The difficulties in measuring tracer trajectories in this region were mainly due to light reflections stemming from the difference between the refractive indices of water, $n \approx 1.33$, and glass, $n \approx 1.51$, and the curvature of the glass pipe. Light reflections deteriorate the contrast between tracers and background. However, the fluid flow could also be measured for $r/R > 0.6$ despite the lower number of usable tracers there. The measured concentration of tracers is roughly linear from $r/R = 0$ to 0.6 and decreases towards the wall for $r/R > 0.6$ for all flow cases. In Oliveira et al. (2013), Eulerian statistics of a single-phase turbulent pipe flow acquired by 3D-PTV have been found to be trustworthy in the near-wall zone if the number of velocity vectors per radial bin exceeds 1000. The same criterion is also applied in the present work.

In the detection of inertial particle trajectories, the above contrast problem between particles and background did not occur. The bigger imaging projection area of inertial particles on the camera sensor, exceeding the projection of tracers by a factor of 16, avoided problems on the identification of particles. While the projection of a tracer image occupies nearly an area of 2×2 pixels, the projection of an inertial particle occupies 8×8 pixels. Roughly, every 3D inertial particle position identified in the tracking algorithm corresponds to a real particle. On average, approximately 3×10^5 inertial particle positions have been identified in each particle-laden case. 3D particle positions were identified with a camera frame rate of 50 Hz in average time intervals of 50 min. In this period, a water volume corresponding to $\approx 2.3\ \mathrm{m}^3$ crosses the test section. In this way, accurate measurements of concentration profiles of inertial particles have been obtained.

Throughout this article, the errors of time-averaged values of a measured quantity x are estimated with the aid of the so-called standard error, σ_m. Confidence intervals of 95% are considered. For a quantity which is measured n times, with instantaneous results x_i and mean $\langle x \rangle$, the standard error is given by:

$$\sigma_m = \sum_{i=1}^{n} [(x_i - \langle x \rangle)^2 / n(n-1)]^{0.5} \tag{5}$$

The effect of the flow orientation with respect to gravity on the concentration profiles of inertial particles, $\Phi_v(r/R)$, is made clear in Fig. 2. Let k represent the total number of radial bins, here 50. In order to determine $\Phi_v(r/R)$, radial bins are defined by $i\Delta r \leqslant r \leqslant (i+1)\Delta r$, with $i \in [0, \mathrm{k}-1]$ being the bin number and with $\Delta r = R/k$. The time-averaged volume of particles within the volume of the bin element i is given by $\Phi_v(i)$; see Eqs. (6) and (7):

$$\langle N_i \rangle = (1/m) \sum_{j=1}^{m} N_i(j) \tag{6}$$

$$\Phi_v(i) = \langle N_i \rangle (Vp/Vi) \tag{7}$$

where j numbers photographs and m is the total number of photographs. Each subscript i corresponds to a radial bin, r. The ratio i/k corresponds to r/R in dimensionless form. The term $\langle N_i \rangle$ represents the time-averaged number of particles in a discrete radial bin, V_p denotes the volume of a particle and V_i the volume of the bin. The mean concentration of inertial particles, $\langle \Phi_v \rangle$, refers to the mean of $\Phi_v(i)$ in all bins, Eq. (8).

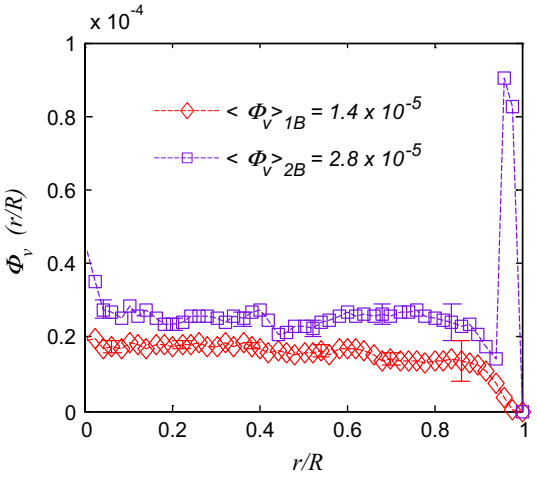

Fig. 2. Effect of the flow orientation with respect to gravity on the concentration profiles of inertial particles, $\Phi_v(r/R)$, in upflow case 1B and in downflow case 2B. For case 1B, the mean volumetric concentration, $\langle\Phi_v\rangle$, is 1.4×10^{-5} and for case 2B, 2.8×10^{-5}. Dashed lines are added to guide the eye. Error bars indicate $2\sigma m$.

$$\langle\Phi_v\rangle = (1/k)\sum_{i=0}^{k-1}\Phi_v(i) \tag{8}$$

Close to the pipe walls in upflow ($r/R > 0.85$), Φ_v decreases with decreasing distance to the wall. Same trends for the concentration profile of case 1B are found for upflow cases 1A/1C. Higher concentrations of inertial particles in the pipe center were also found for gas–solid upward flows by the numerical computations of Kartusinsky et al. (2009). For downflows, there is a concentration peak at about $r/R \approx 0.98$. This trend is also found for downflow case 2A. Similar concentration profiles of inertial particles in downward flow was experimentally obtained by Suzuki et al. (2000), where ceramic beads with mass density exceeding the carrier-phase (water) by a factor of 3.85 have been applied in down-flow, resulting in a maximum concentration of inertial particles at the channel walls (exceeding 7–8 times the concentrations at the channel core). We can conclude that the direction of the vertical flow, upward or downward, strongly affects the concentration profile, $\Phi_v(r/R)$, particularly in the near-wall zone ($0.8 < r/R < 1$). Notice that lift forces can be of relevance for determining the concentration of particles in wall-bounded flows. However, most numerical studies in literature consider small heavy particles only, for which the lift force can be neglected. This leads to different particle behavior than the case of large, almost neutrally buoyant particles which it is considered in this work; see for example Yamamoto et al. (2001) and Wang and Squires (1996).

Particles lighter than the carrier phase (*e.g.* spherical bubbles in liquid flow) are expected to possess rather different concentration profiles to those of heavy particles. In the theoretical analysis of Drew and Lahey (1982), the concentration profile of bubbles in pipe flow showed wall-peaking for up-flow and core-peaking for down-flow. Therefore, the mass densities of the carrier phase and of the particles are also relevant for determining the radial distribution of particles in pipes. These predictions of bubble concentration profiles are confirmed by many experimental results, for example by Zun (1980).

A summary of the results for the concentration is provided in Table 3. Some ratios are useful to characterize the concentration profiles in the present experiments. For example, the ratio of the maximum concentration found in a discrete bin to the mean concentration, $\Phi_{v,\max}/\langle\Phi_v\rangle$, and the ratio of the mean concentration in $0 < r/R < 0.8$ to that in $0.8 < r/R < 1$, R_Φ. Both $\langle\Phi_v\rangle_{(0<r/R<0.8)}$ and $\langle\Phi_v\rangle_{(0.8<r/R<1)}$ are computed according to Eq. (8), but in the indicated parts of the measurement section volume. More information about the concentration profiles of inertial particles is given in Oliveira et al. (2013).

Table 3
Results of the inertial particle concentrations for the particle-laden pipe flow experiments.

Case	Flow direction	$\langle\Phi_v\rangle\cdot10^{-5}$	$R_{\Phi*}$	$\Phi_{v,\max}/\langle\Phi_v\rangle$	$r_{\max}/R$
1S	Upward	0			
1A	Upward	0.5	1.72	1.51	~0
1B	Upward	1.4	1.75	1.42	~0
1C	Upward	3.2	1.65	1.25	~0
2S	Downward	0			
2A	Downward	1.8	0.75	3.55	~0.98
2B	Downward	2.8	0.81	3.21	~0.98

3.2. Mean axial velocity profiles

Criteria for particle break-up depend on the turbulence dissipation rate. Since this quantity cannot be measured directly by means of 3D-PTV, as it involves spatial derivatives of the velocity, we estimate it by the turbulence production. The turbulence production depends on the cross component of the Reynolds stress tensor and the radial derivative of the mean axial velocity component. Therefore, in this sub-section we study the mean axial velocity component and in the next the cross component of the Reynolds stress tensor. In particular, we assess the effects of inertial particle distribution and flow direction on the mean velocity profile.

Inertial particle and tracer trajectories have been registered by 3D-PTV at a camera frame rate of 50 Hz. On average, 2×10^6 velocity vectors for tracers and 3×10^5 for inertial particles have been obtained for each particle-laden case. The velocity vectors are ensemble-averaged in distinct radial bands, which have a discrete width of 1.0 mm around a chosen radius, see Section 3.1.

The effect of upflow direction on the mean axial velocity profiles of fluid, $\langle U_z\rangle$, is presented in Fig. 3. The flow bulk velocity, U_b, was adjusted to keep the same Re_b for each experiment, 10,300. The bulk velocity U_b normalizes the velocity profile. In each plot, the measured single-phase velocity profile is also shown as a reference. Error-bars in Fig. 3 have same sizes as the symbols.

To check the mean axial fluid velocity profiles of particle-laden cases the following procedure was followed. For each fluid flow profile, the mean volumetric flow rate, Q, was determined by integrating $\langle U_z\rangle_i A_i$, over the radius of the pipe. Temperature measurements yielded the water mass density, ρ_f. The product $\rho_f Q$ gives the mass flow rate for each experimental set, which corresponded to the ones given by the Coriolis meter within its inaccuracy range.

In Fig. 3, the mean axial velocity profile for tracers in case 1B is presented. Comparison of mean axial fluid velocities for single-phase and two-phase flows, cases 1S and 1B, indicates a slight reduction in the mean flow velocity in the range $0 < r/R < 0.93$. This reduction is compensated by an increase in mean fluid velocity in the range $0.93 < r/R < 1$, see Fig. 3b. Similar modifications to the mean axial fluid velocity of particle-laden case 1B are found for upward cases 1A/1C. The minor effect of solid particles on the mean liquid velocity was also shown by Sato and Hishida (1996) and by Borowsky and Wei (2007) in wall-bounded flows, particularly if low mean volumetric loads of solids are present (*e.g.* less than 10^{-4}). The prior experimental results are in agreement with the gas–solid channel flow computations of Arcen et al. (2006) and with the computations for pipe flows by Mandø et al. (2009).

The small change in the fluid mean velocity profiles observed above is also apparent in the mean strain rate. Fig. 4 shows the effect of up- or downflow on the mean strain rate, $\partial\langle U_z\rangle/\partial r$, for

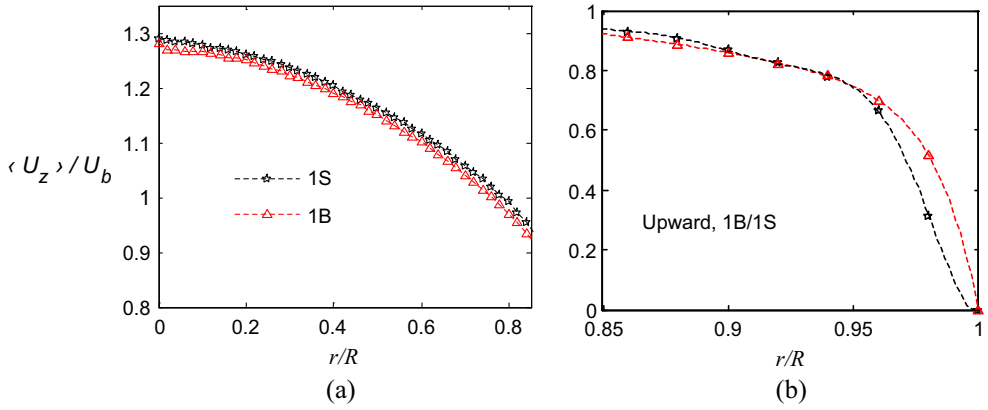

Fig. 3. Mean axial velocity profile, $\langle U_z \rangle$, in upward flow direction of particle-laden case 1B. The velocities are normalized by the bulk velocity of the corresponding flow, U_b. The subscript 1S denotes single-phase flow. In case 1B, the mean volumetric concentration, $\langle \Phi_v \rangle$, is 1.4×10^{-5}. Dashed lines are to guide the eye. Standard error-bars have same sizes as symbols. Fig. 3a presents velocity profiles in the range $0 < r/R < 0.85$ and Fig. 3b in the range $0.85 < r/R < 1$. Each marker corresponds to a bin; notice the difference in scales.

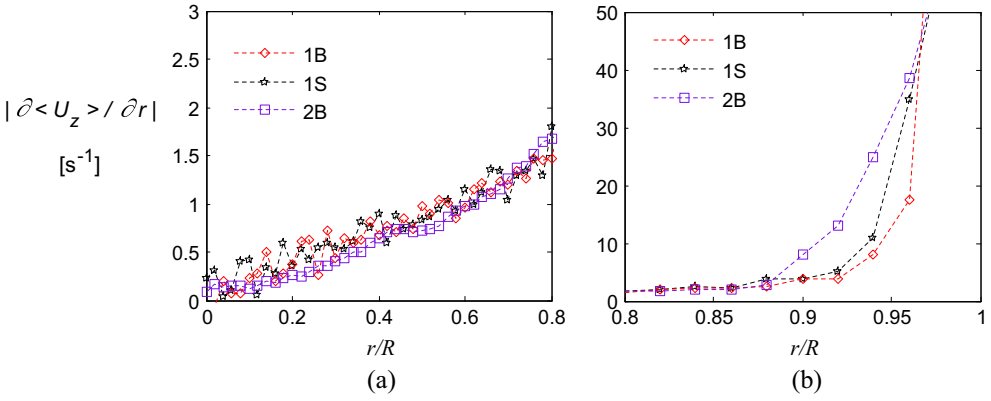

Fig. 4. Effect of the flow orientation with respect to gravity (upflow or downflow) on the mean strain rate, $\partial\langle U_z \rangle/\partial r$, for particle-laden flows 1B and 2B. The subscript 1S denotes single-phase fully developed flow. Dashed lines are added to guide the eye. Each marker corresponds to a bin; notice the difference in scales.

particle-laden flows 1B and 2B. Fig. 4a presents results in the range $0 < r/R < 0.80$ and Fig. 4b, in the range $0.80 < r/R < 1$.

The gradient of the mean strain rate drastically increases at about $r/R \approx 0.88$ for particle-laden downflows and at about 0.92 for particle-laden upflows. For single-phase flows, this happens at $r/R \approx 0.90$. This shift is apparently related to the changes in the mean strain rate profile, which can be understood in terms of local decrease in relative velocity in the following way. In upflows, the drag imposed to the fluid by the heavier particles results in a reduction of the fluid velocity in the pipe core. This reduction is compensated by mass conservation with an increase in the fluid velocity in the near wall-zone. The opposite trend is found in downflows.

3.3. Cross-component of the Reynolds stress tensor

Turbulent stresses are important for particle break-up in the way detailed below, and are part of the Reynolds stress tensor. Let a cylindrical coordinate system with its origin at the pipe centerline and with the axial axis anti-parallel to the gravitational acceleration be defined as in Fig. 5. Let the lower case u indicate the fluctuating fluid velocity component. The effects of flow orientation with respect to gravity (upflow or downflow) and mean volumetric concentration on the cross-component of the Reynolds stress tensor, $\langle u_r u_z \rangle$, are presented in Fig. 6. Results are normalized by the square of the bulk flow velocity, U_b^2, of the

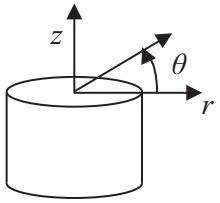

Fig. 5. Cylindrical coordinate system for up- and downward flows. The origin is at the pipe centerline and the axial axis is anti-parallel to the gravitational acceleration.

corresponding experiment. Results for the reference single-phase cross-component are also shown.

In inhomogeneous fully developed pipe flows, the only decoupled direction is the tangential, which means that correlations $\langle u_\theta u_r \rangle$ and $\langle u_\theta u_z \rangle$ are zero. For all measured particle-laden flows, values of cross-components including the tangential direction have been verified to be close to zero.

In Oliveira et al. (2013), results of the single-phase fully developed flow, case 1S, have been compared to the DNS results of Veenman (2004). The 3D-PTV data of case 1S showed good agreement with these DNS results within the measurement error. The cross component of the Reynolds stress tensor of the fluid velocity also showed good agreement between cases 1S and 1B (Fig. 6a). Results for cases 1A/1C are similar to the ones of 1B. For

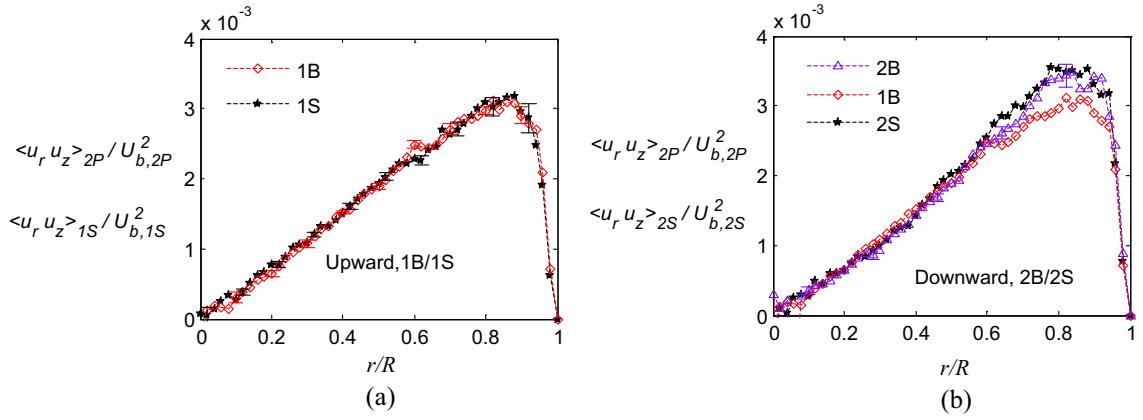

Fig. 6. Effects of the mean concentration, $\langle \Phi_v \rangle$ and flow orientation with respect to gravity (upflow or downflow) on the cross-component of the Reynolds stress tensor, $\langle u_r u_z \rangle$, for particle-laden flows 1B and 2B. Results are normalized by $U_b{}^2$. The subscripts 1S and 2S denote single-phase reference flows and 2P, tracers in two-phase flow. Dashed lines are added to guide the eye.

particle-laden pipe flows in upward direction with $\langle \Phi_v \rangle < 3.2 \times 10^{-5}$, the flow turbulence is barely modified by the presence of the inertial particles. The minor effect of solid particles in $\langle u_r u_z \rangle$ was also observed by Suzuki et al. (2000) in a water channel flow with mean concentration of particles about 3.2×10^{-4}. Vreman (2007) analyzed turbulence characteristics of particle-laden pipe flows by direct numerical simulations of the gas phase and by applying a Lagrangian approach for the solid particles. His results showed that significant changes to the Reynolds stress will be found only for higher concentrations than 5×10^{-3}.

Results of downflows with mean concentration less than 2.8×10^{-5}, cases 2A/2B, are similar to the reference single-phase flow, case 2S. Therefore, only one of them is sufficient to present the main features of $\langle u_r u_z \rangle$. In Fig. 6b, the cross-component profile of case 1B is added to show the differences with upward flows. The discrepancies are particularly pronounced in the range $0.6 < r/R < 0.9$. These small discrepancies are the consequence of the fact that the downflows are close to, but not entirely fully developed yet. A similar observation can be made in Fig. 6b. Although the differences are only minor, their consequences for break-up criteria will be investigated below.

A summary of the results obtained for the cross-component of the Reynolds stress tensor is found in Table 4. Cross-section averaged ratios of present particle-laden flows to the corresponding single-phase references (cases 1S and 2S) are shown for $\langle u_r u_z \rangle$. Results are normalized by $U_b{}^2$. The cross-section averaging is performed according to Eq. (9):

$$\overline{\langle u_r u_z \rangle} = \frac{\int_0^R \langle u_r u_z \rangle 2\pi r dr}{\pi R^2} \tag{9}$$

Table 4 clearly shows that the mean cross-component of the Reynolds stress tensor is barely modified by the presence of inertial particles at the given concentrations and flow conditions. All particle-laden flows with $\langle \Phi_v \rangle$ less than 3.2×10^{-5} present similar results for $\langle u_r u_z \rangle$.

3.4. Production of turbulence kinetic energy

As will be seen in Section 3.5, the production of turbulence kinetic energy is important for the appraisal of conditions for particle break-up. The production of kinetic energy is in a Cartesian coordinate system, $\{x_j\}$, given by:

$$P_k = -\sum_i \sum_j \langle u_i\, u_j \rangle \frac{\partial \langle U_i \rangle}{\partial x_j} \tag{10}$$

Table 4
Cross-section averaged ratios of the cross-components of the Reynolds stress tensor.

Case	1A	1B	1C	2A	2B
$\frac{\overline{\langle u_r\ u_z \rangle}/U_b^2]_{2P}}{\overline{\langle u_r\ u_z \rangle}/U_b^2]_{1P}}$	1.01	1.01	1.02	1.01	1.00

For pipe flows not far from a fully developed condition, the only contributing component is $-\langle u_r u_z \rangle \partial \langle U_z \rangle / \partial r$. The effects of the flow orientation with respect to gravity (upflow or downflow) and mean volumetric concentration on the turbulence production, P_k, for particle-laden flows 1B and 2B are presented in Fig. 7. Results are normalized by the cube of the bulk velocity of each flow divided by the pipe radius, $U_b{}^3/R$. Results for the reference single-phase flows cases 1S and 2S are also shown.

Good agreement is found between the results of cases 1S and 1B. Results for case 1B resemble the ones of other particle-laden upflows, cases 1A/1C, which are not shown here. For particle-laden upflows with $\langle \Phi_v \rangle < 3.2 \times 10^{-5}$, the turbulence production is barely modified. An exception is the radial location of the maximum in P_k, which is shifted from $r/R \approx 0.96$ to 0.98 (Fig. 7b).

The effect of the mean concentration, $\langle \Phi_v \rangle$, on the turbulence production, P_k, for particle-laden downflow 2B is presented in Fig. 7c and d. Results for the reference single-phase flow, case 2S, are also shown. The turbulence production profile of case 1B is added to show the differences with upward flow.

Results for cases 2A resemble cases 2B and are not presented. For downflows with mean concentration less than 2.8×10^{-5}, cases 2A/2B, production is enhanced with respect to the reference single-phase flow, case 2S, in the range $0.9 < r/R < 1$. Moreover, the location of the maximum in P_k is shifted from $r/R \approx 0.96$ to 0.94 (Fig. 7d). Consequently, the cross-sectional average value of P_k is increased by 9% in comparison to case 2S and by 19% in comparison to case 1B. The slight increase of P_k, particularly in the near-wall region, was also observed by Suzuki et al. (2000). Apparently, particle volume loads less than 10^{-4} at the given flow characteristics are too low to significantly affect the production term. Following the computations of Vreman (2007), significant modifications to the production term will be found only for particle-laden flows with high volumetric concentration; *e.g.* $\langle \Phi_v \rangle > 10^{-3}$.

A summary of the results obtained for the turbulence production of energy is found in Table 5. Ratios of cross-section averaged results for the production in particle-laden flows to the

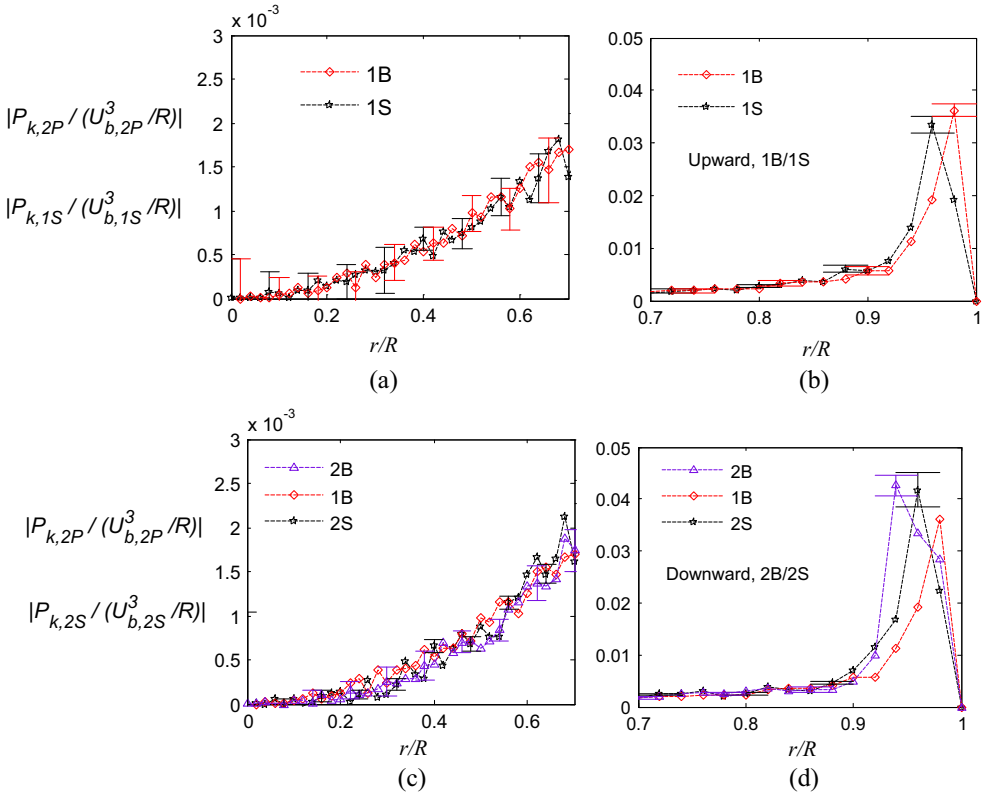

Fig. 7. Effect of the flow orientation with respect to gravity (upflow or downflow) and the mean concentration, $\langle \Phi_v \rangle$ on the turbulence production, P_k, for particle-laden flows 1B and 2B. Results are normalized by $U_b{}^3/R$. The subscripts 1S and 2S denote single-phase reference flow and 2P, tracers in two-phase flow. Dashed lines are added to guide the eye. Each marker corresponds to a bin; notice the difference in scales.

Table 5
Cross-section averaged ratios of the turbulence production.

Case	1A	1B	1C	2A	2B
$\frac{[\overline{P_k}]_{2P}}{[\overline{P_k}]_{1P}}$	1.01	1.02	1.02	1.08	1.09

corresponding single-phase results (cases 1S and 2S) are shown for P_k. The cross-section averaging is performed in the same way as in Eq. (9).

3.5. Direction-dependent Kolmogorov constant

The Kolmogorov constant C_0 is necessary for the evaluation of particle break-up, see Wissen et al. (2004). This Kolmogorov constant can be assessed via the second order Lagrangian velocity structure function, $D_{kk}(\tau)$, which is defined by

$$D_{kk}(\tau) = \langle [u_k(z(\tau),\tau) - u_k(z(0),0)]^2 \rangle \tag{11}$$

where τ is time and u the fluctuating fluid velocity. The subscript k indicates cylindrical components (r, z, θ). Kolmogorov theory of local isotropy gives a scaling rule connecting the fluid structure functions with the universal Kolmogorov constant, C_0; see Pope (2000). The scaling rule is given by Eq. (12):

$$D_{kk}(\tau) = C_0 \langle \varepsilon \rangle \tau \tag{12}$$

where ε is the dissipation rate given by $\varepsilon = 2\nu S_{km}{}^2$, ν is the kinematic viscosity and S_{km} the rate-of-strain tensor. The latter is given by: $S_{km} = (1/2)(\partial U_k/\partial x_m + \partial U_m/\partial x_k)$, with U_k the instantaneous fluid velocity and x_k the spatial coordinate. Eq. (12) is valid in the inertial sub-range for time τ in the interval: $\tau_k \ll \tau \ll \tau_c$. The Kolmogorov time-scale, τ_k, is representative of dissipative scales, while the Lagrangian correlation time, τ_c, is representative of large energy-containing scales. In turbulent flows, τ_k is related to τ_c by the Reynolds number: $\tau_k = \tau_c\ Re^{-1/2}$. Since turbulent pipe flows are inhomogeneous in radial direction, τ_k and τ_c are functions of the radial coordinate. An average estimate for τ_k was computed in Oliveira et al. (2013), roughly 28 ms. For $Re_b = 10{,}300$, that would result in an average estimation of τ_c of 2.8 s.

Due to the hypothesis of local isotropy, turbulence statistics are invariant to rotations and reflections of the coordinate system as long as there is no symmetry breaking by boundary conditions. The local isotropy assumption implies that the structure functions in the three principal directions are equal and therefore C_0 is a constant. At the level of second order statistics, the local isotropy assumption has been very successful for very large Reynolds numbers, see Mydlarski and Warhaft (1998). However, the present Reynolds number is far from this limit. This makes it necessary to introduce a direction-dependent $C_0{}^k$, in the same way as proposed by Pope (2002) in a linear stochastic model for homogeneous shear flow. Later, Walpot et al. (2007) followed the same approach for the definition of C_0 in inhomogeneous pipe flow. According to Kolmogorov similarity, one should observe a plateau of C_0 in the inertial subrange. However, for the limited Reynolds numbers studied here, the inertial subrange has finite width. For finite Reynolds numbers, the plateaus of C_0 may be short or exist only as bumps, see Lien and D'Asaro (2002). Therefore, the value of C_0 will be determined from the maximum in the function of $D_{kk}(\tau)/\langle \varepsilon \rangle \tau$.

In the remainder of this section, the same approach will be applied to determine the Kolmogorov constant for flows laden with inertial particles. The Lagrangian structure function for the radial velocity component scaled with $\langle \varepsilon \rangle\ \tau$ is presented at $r/R = 0.7$ in Fig. 8. The calculation of $D_{kk}(\tau,r)$ is done by averaging over flow

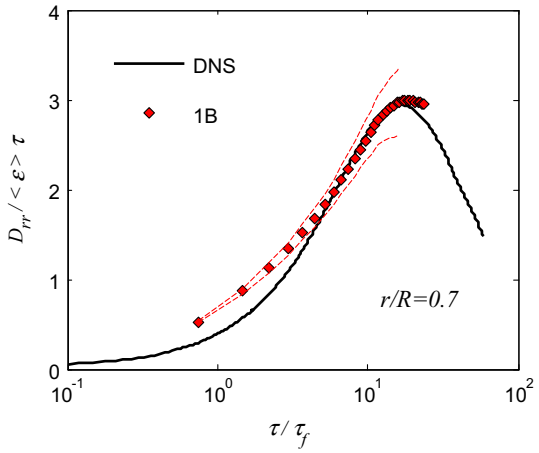

Fig. 8. Lagrangian structure function for the radial velocity component scaled with $\langle\varepsilon\rangle\ \tau$ at $r/R = 0.7$ for case 1B, with inertial particles. The solid line represents single-phase DNS at $Re_b = 10300$. Dashed lines indicate error-bars.

tracers that are situated inside a discrete band centered at a radial position r. The solid line represents single phase DNS data (Veenman, 2004). Diamonds represent flow tracers in particle-laden pipe flow for case 1B at $Re_b = 10{,}300$. Dashed lines indicate error-bars.

Sufficiently long trajectories of tracers have been registered to achieve the time interval where the maximum occurs; see Fig. 8. The value of ${C_0}^k$ is the value of $D_{rr}/\langle\varepsilon\rangle\tau$ at the maximum. Similar results are found at other radial positions and for tangential structure functions. For axial structure functions, the Lagrangian correlation times are bigger and the time interval where the maxima occur cannot be achieved due to the limited axial size of the measurement volume. To overcome this, the axial structure functions are fitted with a linear function in a time interval that is assumed to be in the inertial range; see Walpot et al. (2007) and Oliveira (2012). Results for the ${C_0}^k$ are provided in Fig. 9. Values of ${C_0}^k$ are roughly 3 in the pipe core ($r/R < 0.8$) and somewhat smaller near the wall. These results for flows laden with inertial particles are close to the single-phase experimental results of Walpot et al. (2007) and the DNS computations of Veenman (2004). The particle concentrations are apparently low enough not to affect ${C_0}^k$ too much. Moreover, it appears that the differences between the Kolmogorov constants in the three directions are within the measurement inaccuracy.

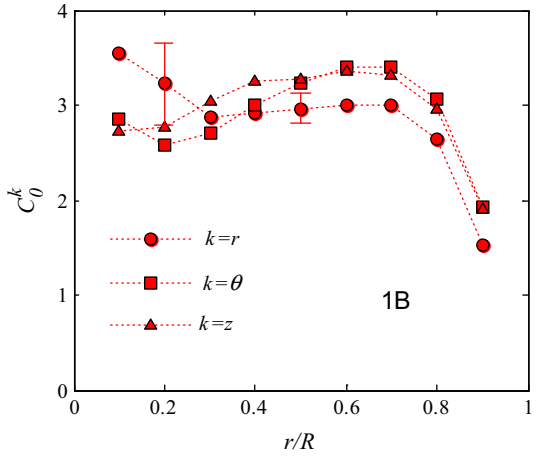

Fig. 9. Direction-dependent Kolmogorov, ${C_0}^k$, constant computed for case 1B. k represents cylindrical coordinates (r, z, θ). Dotted lines are added to guide the eye.

The increase of C_0^k with increasing distance to the wall was also found by Choi et al. (2004) for turbulent channel flow. Walpot et al. (2007) showed that the anisotropy in C_0^k decreases with increasing Reynolds number. There is a generally accepted idea that the Kolmogorov constant increases with increasing Reynolds number and reaches an asymptotic value of approximately 6–7; see Fox and Yeung (2003).

As mentioned in the beginning of this section, C_0 is a quantity necessary to determine break-up criteria. With the above determination of the Kolmogorov constant and turbulence production, all ingredients to derive a break-up criterion for particles in turbulent particle-laden pipe flows are available. This is done in the next section.

4. Particle break-up in turbulent pipe flows

In many processes in the food, dairy and petrochemical industry, small particles occur that have a chance of being torn apart if exposed to too high fluid stresses. The prediction of these processes is of utmost importance, to prevent damage to starch particles and undesirable food appearance, for example. An example of high stresses, induced by steam injection, and computation of break-up chances of particles is given by Wissen et al. (2004). This section discusses effects of inhomogeneous turbulence in pipe flow on particle break-up mechanisms and will present a way to quantify maximum particle sizes in turbulent pipe flows, based on the measurements done in particle-laden flows at $Re_b = 10{,}300$ shown in the previous section.

In principle, the break-up process of particles in pipe flow is isotropic but depends on the distance to the pipe wall. The prediction of the maximum particle diameter, $d_{p,max}$, in turbulent flows is usually based on the pioneering article by Hinze (1956). If particle sizes are in the inertial subrange, his approach states that a critical value of the Weber number, We_{crit}, exists. This Weber number satisfies

$$\left(\frac{\rho_f}{\sigma We_{crit}}\right)^{3/5} d_{p,\max} = (C_0^*)^{-3/5}\varepsilon^{-2/5} \tag{13}$$

where ρ_f is the mass density of the continuous phase, σ the surface tension coefficient, ε the turbulence dissipation rate and ${C_0}^*$ the Kolmogorov constant. Although several authors, *e.g.* Walter and Blanch (1986) and Hesketh et al. (1987), employed Eq. (13) and proposed various expressions for We_{crit}, no universal correlation for pipe flow seems to be available, and none that is based on measurements of turbulence characteristics in particle laden flow. Naturally, and evidenced by (13), the critical Weber number is a function of particle and fluid properties (Walter and Blanch, 1986; Hesketh et al., 1987), but some proposals for We_{crit} also utilized the bulk flow velocity, see Karabelas (1978) for example. In the present study only local features of the flow will be utilized.

Break-up of particles in flow is more complex when the residence time in a certain area of the flow is in competition with the time necessary for break-up. This may be the case in pipe flow when particles are moving fast through areas with high velocity gradients, as those occurring near the pipe wall (Risso, 2000). If this is the case, particle trajectories and times necessary for break-up must be predicted. It is noted that the residence time of inertial particles in the present study has been found to depend on flow direction with respect to gravity. In upflow, the particle residence time at positions close to the pipe center is bigger than in downflow. Particle trajectory computations will predict particle break-up differently in upflow and downflow. Here we focus on finding a break-up criterion based on (13) and assume that the residence time of inertial particles is sufficient to apply (13) without the need to predict particle trajectories. The terms on the RHS

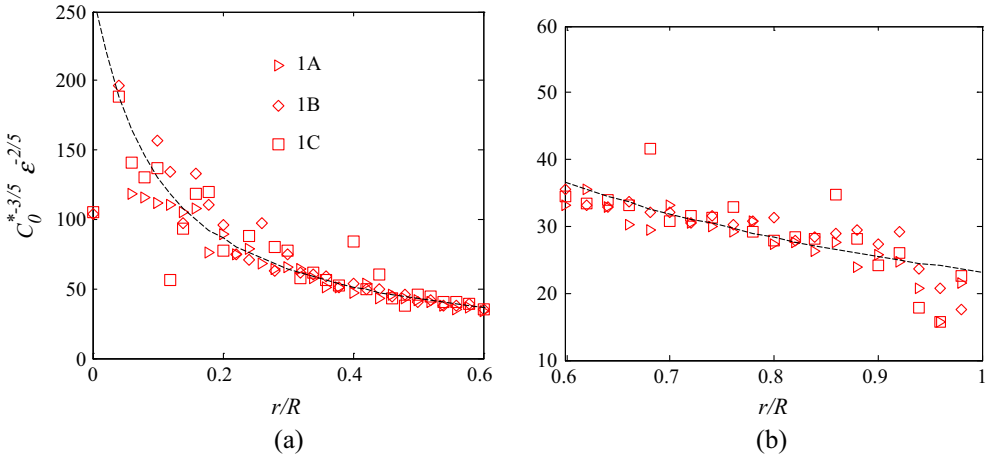

Fig. 10. The effect of inhomogeneous pipe flow turbulence at $Re_b = 10300$ on $C_0^{*-3/5}\varepsilon^{-2/5}$, equivalent to the particle break-up criterion. Turbulence dissipation is estimated from the turbulence production; $\varepsilon \approx P_k$. See Table 2 for the meaning of the flow condition indicators.

of (13) have been evaluated from the measured data presented in the previous section. The results show how the maximum particle diameter depends on radial distance.

In turbulent pipe flows, the turbulence dissipation, ε, occurring in (13) is largest near the wall. Apart from the viscous region near the wall and from a small area in the center of the tube, turbulence dissipation is normally close to the turbulence production, $\varepsilon \approx P_k$. This is clearly shown in the DNS data for the same bulk Reynolds number as in our experiments; see Veenman (2004). The present particle-laden upflow experiments possess all the characteristics of a fully developed single-phase turbulent pipe flow. It is therefore possible to make the comparison of dissipation and production for a single-phase flow with the same bulk Reynolds number. The region near the wall where ε does not agree with P_k is irrelevant since the particle diameter, 0.8 mm, does not permit point force considerations for $r/R > 0.98$. With the above measurements of turbulence production, P_k, and the Kolmogorov constant, ${C_0}^k$, as given in Fig. 9, the RHS of Eq. (13) has been assessed. Values of a modified Kolmogorov constant, ${C_0}^*$, are computed by averaging ${C_0}^z$, ${C_0}^r$ and ${C_0}^\theta$ at each radial bin. The effect of this averaging procedure is an inaccuracy in the Kolmogorov function, C_0, which is negligible as compared to the spread in the results due to the energy dissipation rate, as revealed by Fig. 10 and as quantified by the ${r_s}^2$ and F-values of the fit which are presented below. In Fig. 10, results are shown for particle-laden upflow cases with mean concentration in the range 0.5×10^{-5}–3.2×10^{-5}.

As expected, small values of the quantity ${C_0}^{*\,-3/5}\ \varepsilon^{-2/5}$ are obtained close to the wall, meaning that the maximum particle diameter, $d_{p,max}$, is smaller there: break-up happens more readily near the wall. For given fluid and particle properties, $d_{p,max}$ is larger at the pipe centerline than in the near-wall zone by a factor of more than 5. The scatter in the core of the tube, $r/R < 0.2$, is due to a relatively low number of data points underlying each average given in Fig. 10. This number increases linearly from the pipe axis to r/R about 0.7, levels off and then decreases towards $r/R = 1$ again. In addition, the values of $\partial\langle U_z\rangle/\partial r$ are relatively low in the center of the tube, implying that the relative error is high because of the constant triangulation error.

In downward particle-laden flows, turbulence production is higher in the near wall zone (Fig. 7d), leading to lower values of ${C_0}^{*\,-3/5}\ \varepsilon^{-2/5}$ in Fig. 10b, in particular for the case with the highest loading of inertial particles, case 2b. Since the carrier phase in downflow is not fully developed in this wall zone, the downflow cases are excluded from the following derivation of a break-up criterion for pipe flows, which takes into account the inhomogeneity of the turbulence, based on (13).

A good fit of all experimental data for upflow presented in Fig. 10 turns out to be given by an algebraic function:

$$({C_0}^*)^{-3/5}\varepsilon^{-2/5} = \frac{a_1}{\frac{r}{R} + a_2} \tag{14}$$

The combination of (13) and (14) leads to the break-up criterion:

$$\left(\frac{\rho_f}{\sigma We_{crit}}\right)^{3/5} d_{p,\max} = \frac{a_1}{\frac{r}{R} + a_2} \tag{15}$$

The coefficients for the upflow data are given by: $a_1 = 25.33$ and $a_2 = 0.094$. The quality of the fit is expressed by the two parameters ${r_s}^2$ and F, defined in equations (16) and (17):

$${r_s}^2 = \frac{\sum_{i=1}^{n}(\hat{O}_i - \overline{O})^2}{\sum_{i=1}^{n}(O_i - \overline{O})^2} \tag{16}$$

$$F = \frac{\sum_{i=1}^{n}(\hat{O}_i - \overline{O})^2}{\sum_{i=1}^{n}(O_i - \overline{O})^2}\,\frac{(n-K)}{(K-1)} \tag{17}$$

Here, n is the number of measurements with outcome O_i, $\hat{O}_i$ the predicted values and $\overline{O}$ the mean of the set (O_i). The number of parameters determined in the fit is K.

The values of ${r_s}^2$ and F for the fit (14) are 0.999 and 7729, respectively. These values show that (14) with $a_1 = 25.33 \pm 0.8$ (95% accuracy) and $a_2 = 0.094 \pm 0.004$ (95% accuracy) is a good fit of the data.

When the data for downflow are taken along in the fit, the following values are found: $a_1 = 26.68$ and $a_2 = 0.1216$. The values of ${r_s}^2$ and F for this fit are 0.993 and 6854, respectively. These fit-characteristics are a little bit less because of the spread in the data caused by the downflow data. Comparison of the two fits shows that in particular the value of a_2 depends on the state of development of the flow.

5. Conclusions

Measurements of turbulence production and the Kolmogorov constant as a function of radial distance have been performed in particle-laden turbulent pipe flow. The results enabled the derivation of an empirical correlation for the maximum size a particle will have before break-up will occur. Although the correlation has the familiar form derived by Hinze (1956), it is based on measurements for particle laden turbulent pipe flows with inertial

particles with a Stokes number of 2.3 and mean particle concentrations in the range 0.5×10^{-5}–3.2×10^{-5}. Although the criterion is based on measurements of fully developed upflow, also data for downflow were presented and analyzed. At $Re_b = 10{,}300$ and for given fluid and particle properties, maximum particle sizes at the pipe centerline can be larger than in the near-wall zone by more than a factor of 5.

Although the maximum particle diameter as predicted by the new criterion depends on radial distance, the relationship derived for this radial dependence is because the scaling applied has weak dependence on Reynolds number as long as turbulence production can well be approximated by turbulent dissipation. This implies that the criterion for breakup in pipe flow is expected to be valid for Reynolds numbers exceeding 10,000, as long as volumetric concentrations of inertial particles are low enough to retain the turbulent flow characteristics of single phase flow, *i.e.* $\langle \Phi_v \rangle$ should not exceed (Elgobashi, 1994) 10^{-4}. It is however noted that also the particle residence time can play an important role, see Risso (2000). A particle crossing a free jet with the same (C_0, ε)-values as used in the present investigation but with a small size may therefore not be examined with the particle break-up criterion given by (15) with $a_1 = 25.33$ and $a_2 = 0.094$.

Acknowledgements

The authors gratefully acknowledge support of this work by Brazilian National Council of Research (CNPq) through the project call "Science without borders", protocol number: Proc. 405700/2013-0. Special thanks to Prof. Júlio César Passos from UFSC/Brazil and Dr. Coen Baltis from TUe/Holland. The authors are indebted to Prof. Borée from ENSMA/France for his valuable comments.

References

Albrecht, H.-E., Borys, M., Damaschke, N., Tropea, C., 2003. Laser Doppler and Phase Doppler Measurement Techniques. Springer-Verlag.
Arcen, B., Tanière, A., Oesterlé, B., 2006. On the influence of near-wall forces in particle-laden channel flows. Int. J. Multiphase Flow 32, 1326–1339.
Benson, M., Tanaka, T., Eaton, J.K., 2005. The effects of wall roughness on particle velocities in a turbulent channel flow. ASME J. Fluids Eng. 127, 250–256.
Borée, J., Caraman, N., 2005. Dilute bidispersed tube flow: role of interclass collisions at increased loadings. Phys. Fluids 17, 055108.
Borowsky, J., Wei, T., 2007. Kinematic and dynamic parameters of a liquid–solid pipe flow using DPIV/accelerometry. J. Fluids Eng. 129, 1415–1421.
Caraman, N., Borée, J., Simonin, O., 2003. Effect of collisions on the dispersed phase fluctuation in a dilute tube flow: experimental and theoretical analysis. Phys. Fluids 15, 12.
Choi, J.I., Kyongmin, Y., Changhoon, L., 2004. Lagrangian statistics in turbulent channel flow. Phys. Fluids 16 (3), 779–793.
Clerx, N., van der Geld, C.W.M., Kuerten, J.G.M., 2013. Turbulent stresses in a direct contact condensation jet in cross-flow in a duct with implications for particle break-up. Int. J. Heat Mass Transfer 66, 684–694.
Drew, D.A., Lahey, R.T., 1982. Phase-distribution mechanisms in turbulent low-quality two-phase flow in a circular pipe. J. Fluid Mech. 117, 91–106.
Elgobashi, S., 1994. On predicting particle-laden turbulent flows. Appl. Sci. Res. 52, 309–329.
Fox, R.O., Yeung, P.K., 2003. Improved Lagrangian mixing models for passive scalars in isotropic turbulence. Phys. Fluids 15 (4), 961–985.
Gore, R.A., Crowe, C.T., 1989. Effect of particle size on modulating turbulent intensity. Int. J. Multiphase Flow 15 (2), 279–285.
Hesketh, R.P., Russel, T.W.F., Etchells, A.W., 1987. Bubble size in horizontal pipelines. A.I.Ch.E. J. 33, 663–667.
Hetsroni, G., 1989. Particles–turbulence interaction. Int. J. Multiphase Flow 15 (5), 735–746.
Hinze, J.O., 1956. Fundamentals of the hydrodynamic mechanism of splitting in dispersion processes. A.I.Ch.E. J. 1 (3), 289–295.
Karabelas, A.J., 1978. Droplets size spectra generated in turbulent pipe flow of dilute liquid/liquid dispersions. A.I.Ch.E. J. 24, 170–180.
Kartusinsky, A.I., Michaelides, E.E., Hussainov, M.T., Rudi, Y., 2009. Effects of the variation of mass loading and particle density in gas–solid particle flow in pipes. Powder Technol. 193, 176–181.
Kulick, J.D., Fessler, J.R., Eaton, J.K., 1994. Particle response and turbulence modification in fully developed channel flow. J. Fluid Mech. 277, 109–134.
Kussin, J., Sommerfeld, M., 2002. Experimental studies on particle behaviour and turbulence modification in horizontal channel flow with different wall roughness. Exp. Fluids 33, 143–159.
Lien, R.-C., D'Asaro, E.A., 2002. The Kolmogorov constant for the Lagrangian velocity spectrum and structure function. Phys. Fluids 14 (12), 115–142.
Mandø, M., Lightstone, M.F., Rosendahl, L., Yin, C., Sørensen, H., 2009. Turbulence modulation in dilute particle-laden flow. Int. J. Heat Fluid Flow 30, 331–338.
Marchioli, C., Salvetti, M.V., Soldati, A., 2008. Some issues concerning large-eddy simulation of inertial particle dispersion in turbulent bounded flows. Phys. Fluids 20, 040603. http://dx.doi.org/10.1063/1.2911018.
Miller, R.W., 1996. Flow Measurement Engineering Handbook, third ed. McGraw-Hill.
Mydlarski, L., Warhaft, Z., 1998. Three-point statistics and the anisotropy of a turbulent passive scalar. Phys. Fluids 10 (11), 1–10.
Oliveira, J.L.G., 2012. 3D-PTV of Particle-Laden Turbulent Pipe Flows, Ph.D. Thesis, Technische Universiteit Eindhoven.
Oliveira, J.L.G., van der Geld, C.W.M., Kuerten, J.G.M., 2013. Lagrangian and Eulerian statistics of pipe flows measured with 3D-PTV at moderate and high Reynolds numbers. Flow Turbul. Combust. 91 (1), 105–137.
Paris, A.D., Eaton, J.K., 2001. Turbulence Attenuation in a Particle-Laden Channel Flow. Tech. Rep. TSD-137. Stanford University.
Poelma, C., Westerweel, J., Ooms, G., 2006. Turbulence statistics from optical whole-field measurements in particle-laden turbulence. Exp. Fluids 40 (3), 347–363.
Pope, S.B., 2000. Turbulent Flows. Cambridge University Press, Cambridge.
Pope, S.B., 2002. Stochastic Lagrangian models of velocity in homogeneous turbulent shear flow. Phys. Fluids 14, 1696–1702.
Risso, F., 2000. The mechanisms of deformation and breakup of drops and bubbles. Multiphase Sci. Technol. 12, 1–50.
Sato, Y., Hishida, K., 1996. Transport process of turbulence energy in particle-laden turbulent flow. Int. J. Heat Fluid Flow 17, 202–210.
Schiller, L., Naumann, Z., 1935. A drag coefficient correlation. Z. Ver. Deutsch. Ing. 77.
Suzuki, Y., Ikenoya, M., Kasagi, N., 2000. Simultaneous measurement of fluid and dispersed phases in a particle-laden turbulent channel flow with the aid of 3-D PTV. Exp. Fluids 29, S185–S193.
Tryggvason, G., Bunner, B., Esmaeeli, A., Juric, D., Al-Rawahi, N., Tauber, W., Han, J., Nas, S., Jan, Y.-J., 2001. A front-tracking method for the computations of multiphase flow. J. Comput. Phys. 169, 708–759.
Tsuji, Y., Morikawa, Y., 1982. LDV measurements of an air–solid two-phase flow in a horizontal pipe. J. Fluid Mech. 120, 385–409.
Tsuji, Y., Morikawa, Y., Shiomi, H.H., 1984. LDV measurements of an air–solid two-phase flow in a vertical pipe. J. Fluid Mech. 139, 417–434.
van der Geld, C.W.M., 2002. On the motion of a spherical bubble deforming near a plane wall. J. Eng. Math. 42 (2), 91–118.
Veenman, M.P.B., 2004. Statistical Analysis of Turbulent Pipe Flow: A Numerical Approach, Ph.D. thesis, Technische Universiteit Eindhoven.
Volk, R., Calzavarini, E., Lévêque, E., Pinton, J.-F., 2011. Dynamics of inertial particles in a turbulent von Kármán flow. J. Fluid. Mech. 668, 223–235.
Vreman, A.W., 2007. Turbulence characteristics of particle-laden pipe flow. J. Fluid Mech. 584, 235–279.
Walpot, R.J.E., Rosielle, P.C.J.N., van der Geld, C.W.M., 2006. Design of a set-up for high-accuracy 3D-PTV measurements in turbulent pipe flow. Meas. Sci. Technol. 17, 3015–3026.
Walpot, R.J.E., van der Geld, C.W.M., Kuerten, J.G.M., 2007. Determination of the coefficients of Langevin models for inhomogeneous turbulent flows by three-dimensional particle tracking velocimetry and direct numerical simulation. Phys. Fluids 19, 045102. http://dx.doi.org/10.1063/1.2717688.
Walter, J.F., Blanch, H.W., 1986. Bubble break-up in gas-liquid bioreactors: break-up in turbulent flows. Chem. Eng. J. 32, 7–17.
Wang, L.-P., Maxey, M.R., 1993. Settling velocity and concentration distribution of heavy particles in homogeneous isotropic turbulence. J. Fluid Mech. 256, 27–68.
Wang, Q., Squires, K.D., 1996. Large eddy simulation of particle-laden turbulent channel flow. Phys. Fluids 8 (5), 1207–1223.
Wissen, R.J.E., Schreel, K.R.A.M., van der Geld, C.W.M., 2004. Turbulence production by a steam-driven jet in a water vessel. Int. J. Heat Fluid Flow 25 (2), 173–179.
Yamamoto, Y., Potthoff, M., Tanaka, T., Kajishima, T., Tsuji, Y., 2001. Large-eddy simulation of turbulent gas-particle flow in a vertical channel: effect of considering inter-particle collisions. J. Fluid Mech. 442, 303–334.
Yang, T.S., Shy, S.S., 2005. Two-way interaction between solid particles and homogeneous air turbulence: particle settling rate and turbulence modification measurements. J. Fluid Mech. 526, 171–216.
Zun, I., 1980. The transverse migration of bubbles influenced by walls in vertical bubbly flow. Int. J. Multiphase Flow 6 (6), 583–588.